SINTERING OF HYDROXYAPATITE LATH-LIKE POWDERS

G. C. Koumoulidis[1], *C. C. Trapalis*[2] *and T. C. Vaimakis*[1*]

[1]Department of Chemistry, University of Ioannina, P.O. Box 1186, Ioannina 451 10, Greece
[2]'Demokritos' National Center for Scientific Research, Institute of Materials Science, 153 10 Athens, Greece

Hydroxyapatite powders, which consisted of lath-like single-crystalline particles, were calcined at two different temperatures. Green and calcined powders were used for sintering HAp ceramic samples under uniaxial pressing. Powders and sintered samples were studied using various analytical techniques in order to determine how calcination affects the particle properties and the sintering behavior of HAp powders. It was found that calcination decreases the particles length and changes the particles morphology from lath-like to spherical shape. The relative density increases with increasing calcination temperature and aging time. It was found that long aging time favor the formation of thermally stable HAp particles, whereas a shorter one results in the formation of β-calcium phosphate during thermal treatment. Sintering of compacted powders begins at temperatures greater than 900°C, with a trend to increase the onset temperature as the calcination temperature is increased.

Introduction

Artificially prepared Hydroxyapatite [HAp, $Ca_{10}(PO_4)_6(OH)_2$] has excellent compatibility with the human body due to the similarity of the HAp and natural bone. Porous HAp ceramics have been fabricated using HAp fibers, polycrystalline needle structures, or single-crystalline whiskers and have been widely applied as bone substitutes [1–4]. Physical and chemical properties of HAp ceramics strongly depend on the crystal structure and properties of raw powders [5]. HAp powders are usually calcined at high temperatures before sintering of ceramic. Calcination is applied in order to adjust various powder properties for subsequent processing of HAp ceramics [6]. Recently the model of the grain growth of hydroxyapatite during the sintering was studied [7–9]. Control of particle size and shape as well as particle size distribution and agglomeration, have been widely studied in order to improve the mechanical properties of sintered HAp [10, 11]. The optical transmittance of sintered hydroxyapatite was also studied [12]. Submicron HAp powders are also investigated as they exhibit greater surface area. In particular, nanometer sized HAp is expected to have better bioactivity than coarser crystals. It was found that low temperature of densification prevents the formation of other calcium phosphate phases such as α–tricalcium phosphate (α-TCP) and β-tricalcium phosphate (β-TCP) that may form at sintering temperatures exceeding 900°C [13]. When hot pressing was applied at the sintering process, the decomposition of HAp has not occurred in the temperature range of 1150–1300°C [14]. The sintering temperature is also a critical factor influencing the phase stability, densification behavior, microstructure, and hence the hardness of HAp ceramics. Sintering at elevated temperature tends to eliminate functional OH groups in the HAp matrix (dehydration) and this would result in the decomposition of HAp phase to form α–tricalcium phosphate (α-TCP, high temperature phase modification), β–tricalcium phosphate (β-TCP, low temperature phase modification), tetra-calcium phosphate (TTCP), or oxy-hydroxyapatite (OHAp). For commercial HAp the optimum sintering temperature was found to be 1250°C, and decomposition was observed to occur above 1350°C. The decomposition of HAp was detrimental to sintering, densification and hardness property [15]. Although, the start of shrinkage and the densification of HAp depends mainly on the Ca/P ratio, the final sintering density depends on the particle size, the homogeneity and the agglomeration character of the powder precursor [16].

Recently, HAp lath-like nanoparticles have been prepared using high energy dispersing equipment in combination with pH shock wave method. The particles were single-crystalline, with anisotropic crystal growth and average grain size ca 140–1300 nm in length, 20–100 nm in width and 10–40 nm in thickness [17]. This paper is devoted to study the effect of thermal treatment on the nanoparticles fabrication. HAp powders, dried at 90°C and calcined at two different temperatures before sintering, have been studied using thermogravimetric (TG), differential thermal analysis (DTA), thermomechanical analysis (TMA),

powder X-ray diffractometry (XRD), Fourier-transform infrared spectroscopy (FTIR) and transmission electron microscopy (TEM), in order to investigate how the calcination affects the lath-like particle properties and the sintering behavior of HAp powders.

Experimental

HAp lath-like particles were obtained by the elsewhere described pH shock wave method using high-speed dispersing equipment [17]. An 800 mL solution of ~0.0538 mol $Ca(H_2PO_4)_2 \cdot H_2O$ and ~0.1254 mol $CaCl_2 \cdot 2H_2O$ with a Ca/P molar ratio of 1.67 (the stoichiometry of HAp) was transferred into the reactor vessel and was heated at a temperature of 97±1°C. The rotation speed of the disperser was adjusted at 5000 rpm. Ten mL of condensed ammonium solution (25% w/v) were added. The produced slurry was aged at temperature of 97±1°C, for 0.5, 1 or 2 h. Subsequently, the slurries were cooled to room temperature, filtrated, washed using distilled water and dried at 90°C for 24 h. The precursor amounts, are listed in Table 1 with respect to the aging time. In this table, HAp powders aged for 0.5, 1.0 and 2.0 h are identified as run 1, 2 and 3, respectively. A portion of 1 g of the samples was subsequently calcined for 4 h in an oven at temperature of 550 or 800°C. The calcination temperatures were chosen with respect to thermal data derived from differential thermal analysis (DTA).

TG and DTA analyses of the samples were performed using a NETZSCH simultaneous TG-DTA apparatus (Model STA 449C, Jupiter) from ambient temperature to 1400°C in nitrogen atmosphere (flow rate ~30 mL min^{-1}) with heating rate of β=10°C min^{-1}. The mass of the samples was about 50 mg.

XRD technique was carried out using a BRÜKER D8 ADVANCE diffractometer with secondary graphite monochromator and CuK_α radiation. The measurements were performed using the following combination of slits: 0.6°/0.6°/0.6° as aperture diaphragms. The measured 2θ range was [20–60°], the scan step was 0.02° and the integration time was 1 s per step.

FT-IR spectra were measured using a PerkinElmer, SPECTRUM RX I FT-IR spectrophotometer. The KBr disk technique was employed using 2 mg of HAp powder in 200 mg of spectroscopic–grade KBr (MERK), which had been dried at 100°C. Infrared spectra were recorded in the 4000–400 cm^{-1} region, with resolution of 4.00 cm^{-1}.

Textural studies were performed by transmission electron microscopy using a TEM microscope (Model CM20, Philips). TEM specimens were prepared as follows. The dried powder was added in ethanol and stirred very mildly. A drop of this solution was placed on a Cu grid covered with a C/formvar thin film and was left to dry. Consequently, a dispersion of thin, electron-transparent particles was obtained on the Cu grid and was examined under a transmission electron microscope operated at a 200 kV accelerating voltage.

The density of the green and calcined samples was determined by a Quantachrome stereopycnometer (Model SPY-3). The relative density was calculated from the theoretical density of HAp (3.156 g cm^{-3}).

For sintering analysis, the powder samples were uniaxially pressed in a cylindrical die, with diameter of 6 mm, under a 350 MPa compressing stress. Linear shrinkage and differential linear shrinkage were determined with a NETZSCH horizontal dilatometer (Model TMA/DIL 402C), using the same thermal cycle as the one used for TG-DTA techniques, i.e. a heating rate of 10°C min^{-1}, plus an isothermal stage at temperature of 1400°C. After cooling, the specimens were grinded and the phase analysis was performed by XRD and FT-IR techniques. The peak separation of the differential linear shrinkage curves was performed using NETZSCH SEPARATION OF PEAKS software (SW/PKS/650.01A).

Results and discussion

The chemical analysis results and final Ca/P atomic ratio of the HAp samples are shown in Table 1. The CaO and P_2O_5 contents were smaller than the theoretical values of pure HAp (55.82% CaO and 42.39% P_2O_5). The Ca/P atomic ratio was ~1.66 which was close to the theoretical value (1.67). These results indicate the formation of nonstoichiometric hydrated HAp, whose formula according to literature [18] is

$$Ca_{10-x}(HPO_4)_x(PO_4)_{6-x}(OH)_{2-x} \cdot nH_2O$$

$$0 < x < 1 \text{ and } n = 0–2.5 \tag{1}$$
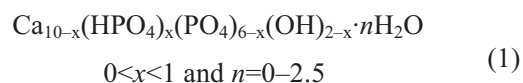
The values of x and n were calculated using the above empirical formula and the chemical analysis results. The acidic group content of HAp was small ($0.027 < x < 0.102$), whereas the bounded water content was significant ($2.72 < n < 4.61$). The amount of bounded water increased as the aging time increased. In our previous work [17], we found that when this kind of HAp was dried for only 3 h, the bounded water amount was also significant (2.945–7.887) and decreased as the aging time increased. These contradictory results indicate that a large portion of bounded water consists of absorbed water, and its amount depends on the experimental procedure.

Figure 1 shows the TG, DTG and DTA curves of uncalcined HAp samples obtained for different aging time (0.5, 1.0 and 2.0 h). The thermal transformation takes place through four consecutive steps. The first

166

**Table 1** Experimental conditions, composition, and molecular formula of HAp powders

Run	Reagent mass/g		Aging time/h	HAp composition Measured		Atomic ratio, Ca/P		$Ca_{10-x}(HPO_4)_x(PO_4)_{6-x}(OH)_{2-x} \cdot nH_2O$ Measured	
	$Ca(H_2PO_4)_2 \cdot H_2O$ (±0.0001 g)	$CaCl_2 \cdot H_2O$ (±0.0001 g)		$CaO/\%$ (±0.02)	$P_2O_5/\%$ (±0.02)	Nominal (±0.001)	Measured (±0.001)	x	n
1	13.5026	18.3759	0.5	52.98	40.61	1.667	1.6571	0.096	2.72
2	13.5019	18.3752	1.0	51.62	39.29	1.667	1.662	0.027	4.46
3	13.5034	18.3750	2.0	51.30	39.35	1.667	1.650	0.102	4.61

Table 2 Mass loss/% observed during the different steps depicted from thermogravimetric data (Figs 1, 2)

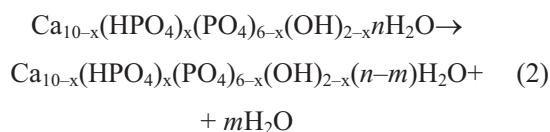| Stage	1st	2nd	3rd		4th	Total		
Temperature/°C	Ambient–130	130–720	720–1320		1320–1400	Ambient–1400	Ambient–550	550–800
			720–890	890–1320				
Aging time/h			Mass loss/%					
0.5	0.37	2.89	0.34	0.86	0.13	4.59	3.07	0.42
1.0	0.58	3.16	1.25		0.21	5.20	3.72	0.27
2.0	0.82	3.15	1.28		0.19	5.44	3.66	0.27

Table 3 Dilatometric results for powders aged for various times and calcined or not at 550°C and 800°C

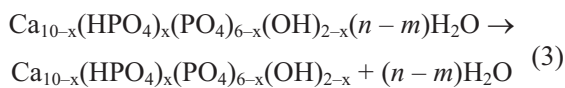| Aging time/h	Un-calcined					Calcined at 550°C					Calcined at 800°C				
	dL/L_0/%	Temperature/°C			dL/L_0	dL/L_0/%	Temperature/°C			dL/L_0	dL/L_0/%	Temperature/°C			dL/L_0
		Onset	Endset	Width	Width/β /%°min⁻¹		Onset	Endset	Width	Width/β /%°min⁻¹		Onset	Endset	Width	Width/β /%°min⁻¹
0.5	−14.84	972	1230	258	−0.575	−18.76	998	1258	260	−0.722	−15.57	1001	1209	208	−0.748
1	−14.90	934	1207	273	−0.546	−16.97	929	1224	295	−0.575	−15.83	1034	1246	212	−0.747
2	−14.81	993	1257	264	−0.561	−16.20	1007	1252	245	−0.661	−16.10	1009	1205	196	−0.821
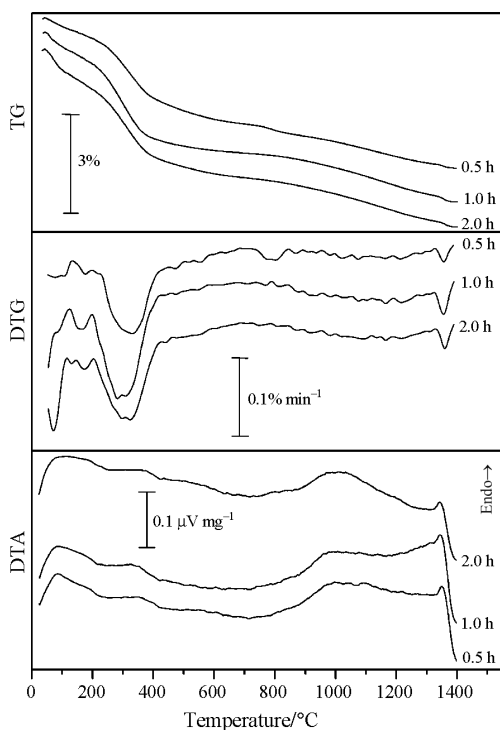
Fig. 1 TG, DTG and DTA curves of HAp powders. The aging time is indicated

step is endothermic, takes place between room temperature and about 130°C and it can be attributed to the removal of absorbed water.
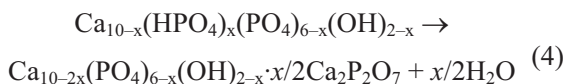
$$Ca_{10-x}(HPO_4)_x(PO_4)_{6-x}(OH)_{2-x}nH_2O \rightarrow$$
$$Ca_{10-x}(HPO_4)_x(PO_4)_{6-x}(OH)_{2-x}(n-m)H_2O+ \quad (2)$$
$$+ mH_2O$$

The mass loss for this step is 0.36, 0.58 and 0.72% for samples with aging time of 0.5, 1 and 2 h respectively, which suggests an increasing water adsorption tendency as the aging time is increased. These results are in accordance with the calculated bounded water n, shown in Table 1.

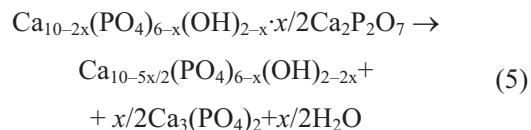The removal of residual crystalline water $((n-m)H_2O$ in reaction (3)

$$Ca_{10-x}(HPO_4)_x(PO_4)_{6-x}(OH)_{2-x}(n-m)H_2O \rightarrow$$
$$Ca_{10-x}(HPO_4)_x(PO_4)_{6-x}(OH)_{2-x} + (n-m)H_2O \quad (3)$$

and the transformation of acid-phosphate to pyro-phosphate take place between 130

$$Ca_{10-x}(HPO_4)_x(PO_4)_{6-x}(OH)_{2-x} \rightarrow$$
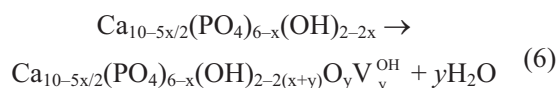$$Ca_{10-2x}(PO_4)_{6-x}(OH)_{2-x}\cdot x/2Ca_2P_2O_7 + x/2H_2O \quad (4)$$

and 720°C, during a second endothermic step. The mass loss of this second step is 2.88, 3.12 and 3.20% for the samples with aging time of 0.5, 1 and 2 h, respectively. The main loss occurs up below 400°C with a

mass loss of about 2.35, 2.81 and 2.77% respectively. The mass loss for temperature range from 400 to 720°C is 0.53, 0.30 and 0.43%. This anomalous tendency indicates that the equilibrium on the slurry continued at least up to 2 h.

A continuous and slow mass loss take place between 720 and 1320°C, during a third endothermic step, which is attributed to the transformation of pyro-phoshate to HAp
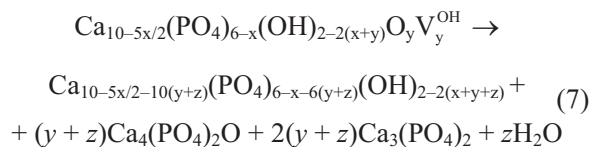
$$Ca_{10-2x}(PO_4)_{6-x}(OH)_{2-x}\cdot x/2Ca_2P_2O_7 \rightarrow$$
$$Ca_{10-5x/2}(PO_4)_{6-x}(OH)_{2-2x}+ \quad (5)$$
$$+ x/2Ca_3(PO_4)_2+x/2H_2O$$

together with the partial dehydration of HAp

$$Ca_{10-5x/2}(PO_4)_{6-x}(OH)_{2-2x} \rightarrow$$
$$Ca_{10-5x/2}(PO_4)_{6-x}(OH)_{2-2(x+y)}O_yV_y^{OH} + yH_2O \quad (6)$$

where V^{OH} denotes the lattice vacancies on OH sites. The weak and broad peak at about 800°C, on the DTG curve of the sample with aging time of 0.5 h, indicates the easy out-diffusion of vapors from bulk sample. This peak is not observed for samples with large aging time. As the aging time is increased, the surface of non- stoichiometric HAp is presumably converted faster to a stoichiometric HAp layer. This stoichiometric layer hinders the out-diffusion of water vapor.

The fourth step is taking place at higher temperatures where the HAp is decomposed to tri-calcium phosphate and tetra-calcium phosphate.

$$Ca_{10-5x/2}(PO_4)_{6-x}(OH)_{2-2(x+y)}O_yV_y^{OH} \rightarrow$$
$$Ca_{10-5x/2-10(y+z)}(PO_4)_{6-x-6(y+z)}(OH)_{2-2(x+y+z)}+ \quad (7)$$
$$+ (y+z)Ca_4(PO_4)_2O + 2(y+z)Ca_3(PO_4)_2 + zH_2O$$

Weak but sharp peaks observed on the DTG curves indicate that the decomposition is almost complete at 1400°C. The DTA curves initially show, an endothermic effect, which is followed by an exothermic tendency above 1355°C. The exothermic tendency is attributed to crystallization of the tri-calcium phosphate and tetra-calcium phosphate. The maxima of the endothermic peaks are located at 1341, 1343 and 1350°C for samples with aging time of 0.5, 1 and 2 h respectivelly, which indicates the increasing stability of HAp as the aging time is increased.

In order to study the products of reactions 3 and 4, powder samples were calcined at constant temperatures of 550 and 800°C. The optimum time of calcination was determined from the stepwise thermogravimetric analysis shown in Fig. 2. The stepwise thermal decomposition of the sample with aging time of 0.5 h (run 1) shows that the mass loss during the first thermal step is 3.07 and 0.42% during the second
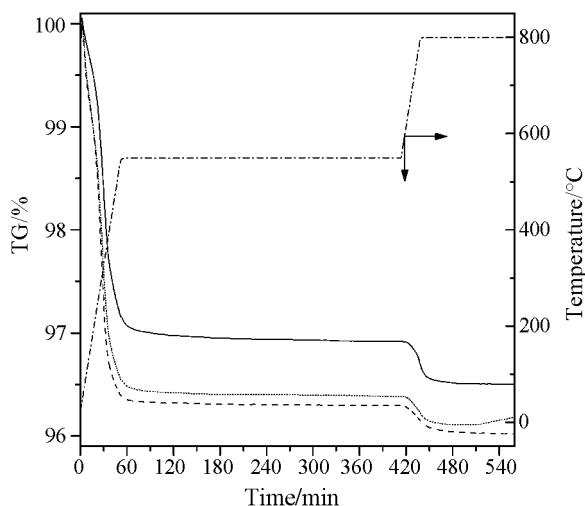
Fig. 2 Stepwise thermogravimetric analysis of HAp powders. Aging time: 0.5 h (—), 1.0 h (– – –), 2.0 h (····) and (– · –) temperature

one (Table 2). The decomposition behaviour of the samples with aging time of 1 and 2 h (runs 2 and 3, respectively) is very close. For the first step the mass loss was about 3.7%, and for the second one it was 0.27%. From the mass losses described in Table 2 the similar behavior the runs 2 and 3 is evident.

Figure 3 shows the XRD patterns of 90°C dried and 550, 800 and 1400°C calcined HAp powders, for aging times of 0.5 (run 1) and 2 h (run 3). As it can be seen, the XRD patterns of samples dried at 90°C and

samples calcined at 550°C, show strong and sharp peaks, which correspond to highly crystalline HAp (File No. 73-0293, International Center for Diffraction Data, ICDD). The absence of extraneous peaks indicates that a pure HAp is formed. When increasing the calcination temperature up to 800°C, a small amount of α-calcium phosphate (high temperature phase modification – $Ca_3(PO_4)_2$, α-TCP, File No. 70-0364, ICDD) was detected for the HAp sample of run 3. For the sample of run 1 a small amount of β-calcium phosphate (low temperature phase modification – $Ca_3(PO_4)_2$, β-TCP, File No. 70-2065, ICDD) also appears in addition to α-calcium phosphate crystalline phase. This result demonstrates that powders with shorter aging time show lower stability during thermal treatment. The XRD patterns of specimens sintered at 1400°C show that the α-TCP is the main phase irrespective of aging time. After this high temperature thermal treatment, the HAp phase almost disappears, while a new phase of tetra-calcium phosphate (Hilgenstockite, $Ca_4(PO_4)O$, File No. 70-1379, ICDD) is detected. For all the thermal treatment, powder of run 2 exhibited trend similar to powder of run 1.
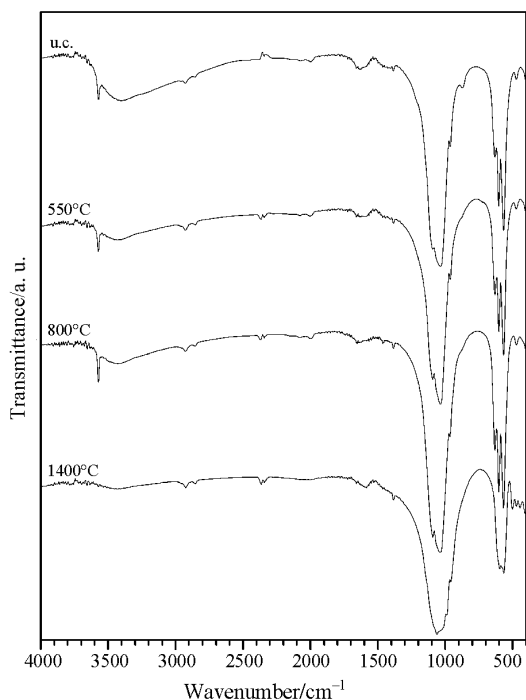
Figure 4 shows the FTIR absorption spectra of run 1 HAp powders, dried at 90°C and calcined or not powders at 550, 800 and at 1400°C. In general, the spectra are in accordance with those reported in the literature of HAp [18–19]. The broad band at 3100–3500 cm^{-1} corresponds to adsorbed
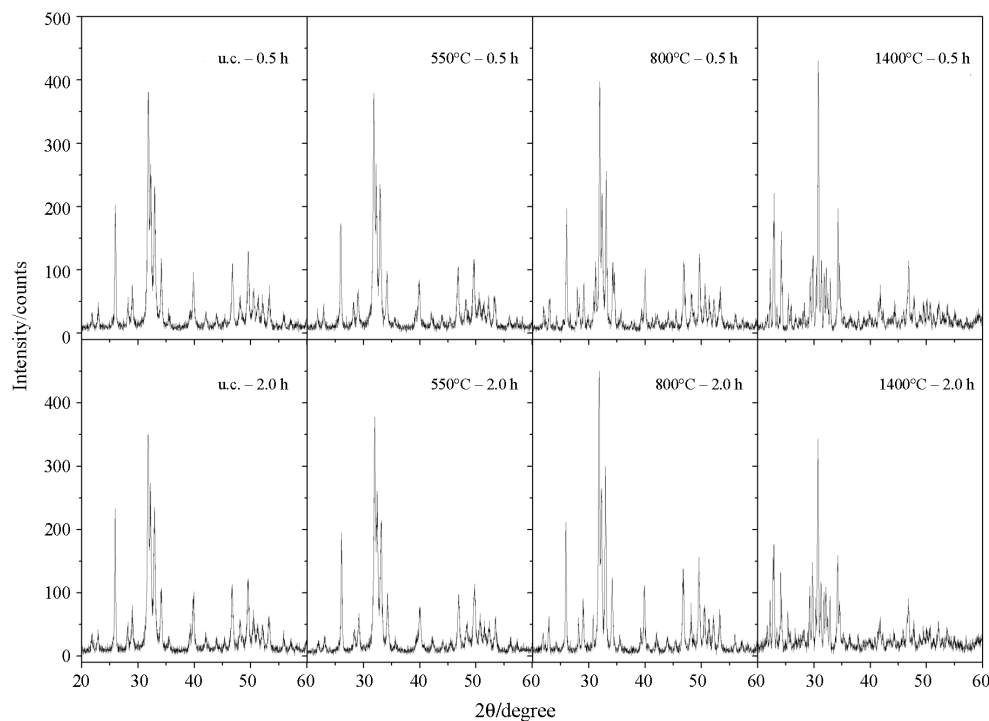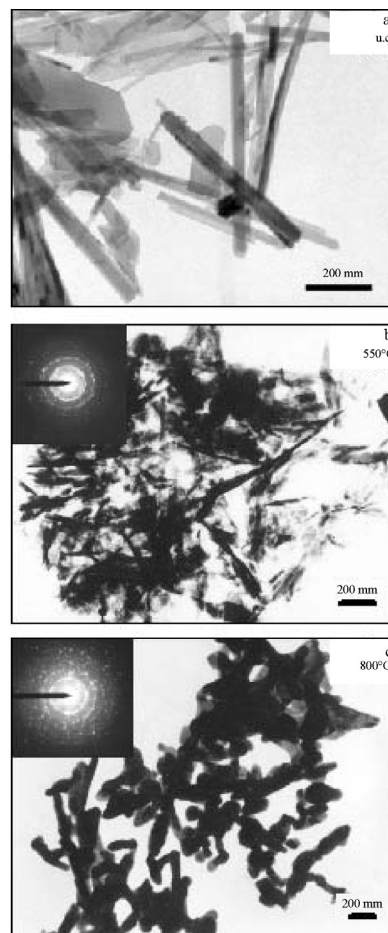

Fig. 3 XRD patterns of green and calcined HAp powders. The aging time and calcination temperatures are indicated (u.c. – accounts for uncalcined sample)

hydrate [20], which is observed to progressively disappear as the processing temperature is increased. However the total intensity of this band is about the same, for samples calcined at 550 and 800°C, due to their similar composition, i.e. similar absorption properties and hence the same amount of absorbed atmospheric humidity. A weak and sharp peak located around ~3570 cm^{-1} corresponds to the stretching vibration of the lattice OH$^-$ ions [20]. This peak disappeared after calcination at 1400°C, which corroborates the disappearance of the HAp phase depicted by XRD. The weak shoulder located at ~1255 cm^{-1} and a weak peak at 880 cm^{-1} can be assigned to P–O–H in plane and out of plane deformation mode, respectively, which indicates the presence of ionic HPO$_4^{2-}$ groups, i.e. the formation of nonstoichiometric HAp. These peaks, of course, only appear in the uncalcined sample. The characteristic bands of PO$_4^{3-}$ groups in HAp appear at 473, 565, 602, 962, 1033 and 1091 cm^{-1} [21]. The medium sharp peak located at 632 cm^{-1} was assigned to the O–H bending deformation mode, and related to the presence of HAp phase. The PO$_4^{3-}$ bands of the sample sintered at 1400°C appear at 464, 596, 956 and 1063 cm^{-1}, which can be attributed to tri- and tetra-calcium phosphate phases. Similar results have been recorded for HAp powders of runs 2 and 3.

Typical TEM bright field micrographs of run 1 HAp powders are shown in Fig. 5 for powders dried at 90°C (Fig. 5a) and powders calcined at 550°C
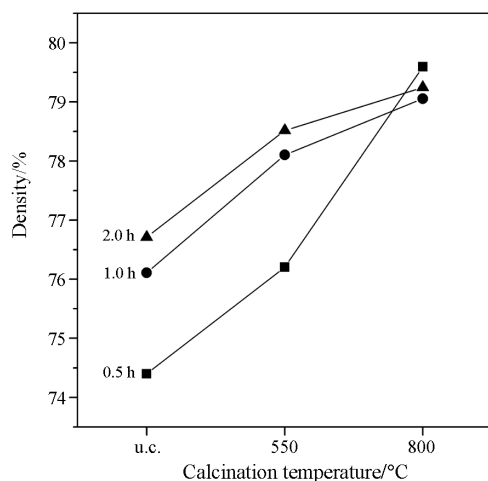

Fig. 5 TEM bright field micrographs of HAp 'lath-like' particles. The thermal treatment temperatures are indicated. Insert in 5b and c shows the associated selected area electron diffraction pattern verifying that the particles are HAp

(Fig. 5b) and 800°C (Fig. 5c). In the inserts of Fig. 5b and c the associated selected area electron diffraction patterns are shown. Indexing of the diffraction rings proves that both of samples consisted of HAp crystals, which is in agreement with the X-ray diffraction results. As can be seen in the Fig. 5a, the as-dried HAp powder forms bundles of thin elongated lath-like particles with length between 200 and 1300 nm and thickness between 10 and 40 nm. Similar particles are observed for the sample calcined at 550°C (Fig. 5b)) but their length is significantly reduced.

After calcinations at 800°C (Fig. 5c) lath-like particles still exist but they exhibit more elliptical shape and reduced length. This phenomenon corresponds to coalescence of particles, which was also described in similar calcium deficient HAp powders [21]. Consequently the morphology and the structure of the HAp powders in the as prepared and calcined at 550°C samples are similar to one another and different from the morphology and size of the

Fig. 4 FT-IR spectra of HAp powders. The temperatures of thermal treatment are indicated
(u.c. – uncalcined sample)

Fig. 6 Relative density of HAp powders calcined at various
temperatures. The aging time is indicated

HAp calcined at 800°C. This marked difference is
attributed to the different calcination times and temp-
eratures of the HAp powders.

The effect of calcination temperature on the
relative density is shown in Fig. 6. The relative
density is observed to increase as the calcination tem-
perature and aging time are increased. The relative
density of powder calcined at 800°C was almost the
same for all the samples (about 79.5%). This behavior
could be attributed to the process described thereafter.
These measured densities are lower than the theoreti-
cal value but are in agreement with values reported in
the literature [6].

The linear shrinkage of green HAp and calcined
samples, is illustrated in Fig. 7 and Table 3. In
general, the curves exhibit a sigmoidal shape. They
indicate that sintering begins (onset temperature) at
temperatures ranging from 934 to 1034°C. The onset
temperature is observed to increase as the calcination
temperature was increased. The temperature widths,
which are the temperature ranges from onset to
endset, are almost the same for uncalcined powders
and powders calcined at 550°C, while for samples
calcined at 800°C samples they are about 50 degree
narrower. Landi *et al*. [22] have reported that calcined
powders begin to shrink at higher temperature and
stop to shrink later than uncalcined ones. In our case,
the onset temperatures listed in the Table 3 seem to
agree with the observations of Landi *et al*., while for
the endset temperatures of the samples calcined at
800°C appear to disagree. However, the Fig. 7 shows
that the linear shrinkage of uncalcined samples almost
stopped at the end of the dynamic step, while for
samples calcined at 550 and 800°C, sintering stopped
during the final isothermal step after about 80 and
115 min, respectively.

The final dimension change (the total per cent
linear shrinkage) appeared to be maximum for
samples calcined at 550°C. This behaviour could be
attributed to the dimension and morphology of
primary particles, which would influence the densi-
fication and packing efficiency.

Indeed TEM observation show that, compared to
green powders calcined at 550°C, exhibit lath like but
smaller grains with a larger specific surface and thus a
greater contact surface, which promotes better
sintering features. After calcination at 800°C,
samples show more rounded grains with smaller
contact surface, which would inhibit the sintering
mechanism. Assuming that the shrinkage curve is
nearly straight line, the overall shrinkage rate was cal-
culated from the equation:

$$\text{Shrinkage rate} = \frac{\text{Total linear shrinkage}}{(\text{Temperature width})/(\text{Heating rate})}$$

(8)

As shown in Table 3 the shrinkage rate increased
with increasing the calcination temperature, which is
attributed to the decrease of the particle size and
hence the increase of the contact surface

Figure 8 presents the differential linear shrink-
age of the samples differentiated from the experimen-
tal curves of Fig. 7. From this figure it is evident that
the sintering mechanism takes place in several stages.
The peak separation (deconvolution) of differential
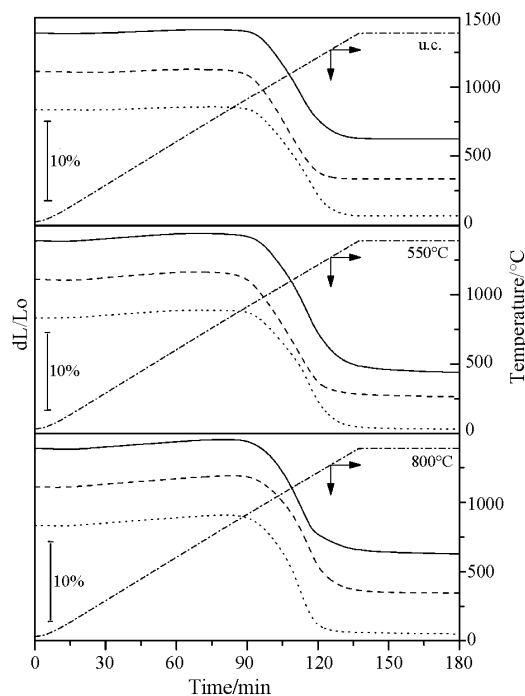
Fig. 7 Linear shrinkage of green and calcined HAp powders.
The calcination temperatures are indicated. Aging time:
0.5 h (—), 1.0 h (– – –), 2.0 h (····) and
– · – temperature (u.c. – uncalcined sample)
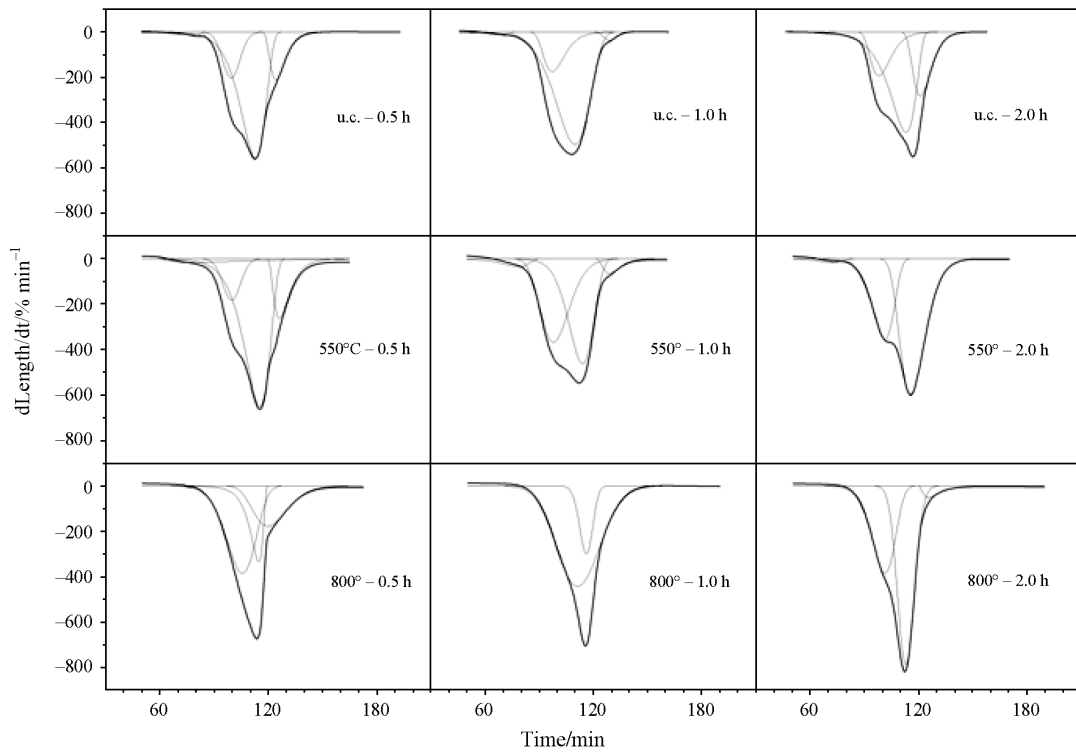
Fig. 8 Peak separation of differential linear shrinkage curves for green and calcined HAp powders. Aging time and calcination temperatures are indicated in the figure (u.c. – uncalcined sample)
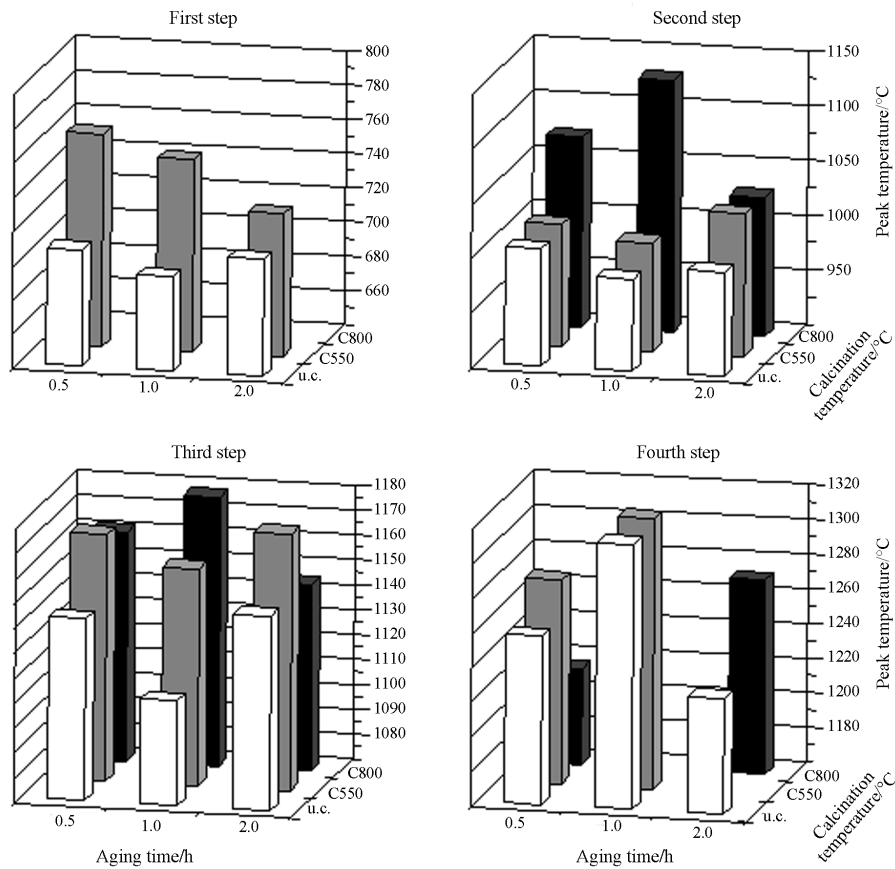
Fig. 9 Temperature peak of the shrinkage stages depicted from Fig. 8 for HAp powders calcined or not at 550 and 800°C with various aging time (u.c. – uncalcined sample)

linear shrinkage provides information on the temperature range (Fig. 9) and relative importance of the different shrinkage stages (Fig. 10). Four stages were evidenced. The first one, only observed for the green samples and samples calcined at 550°C, takes place in a low temperature range below 800°C. The relative shrinkage in this first step was less than 4%. It is attributed to slow dehydroxylation and formation of tri-calcium phosphate due to reaction 5. The accelerated dehydroxylation occurs mainly during the next two stages, in which the reactions 5 and 6 take place and is characterized by an enhanced densification rate [22]. The temperature peaks are about 1050 and 1150°C for the second and third shrinkage stage respectively. According to Ruys *et al.* [23], the HAp densification mainly take place between 900 and 1150°C after what the pore collapse and blowholes appear between 1150–1200°C. In our case, these processes took place during the second and third stages, respectively. Ruys *et al.* also reported that for temperatures ranging between 1200 and 1350°C, the blowholes increase in size and number. In our case, this procedure takes place during the forth stage. Figures 9 and 10 also show that, during the second stage, the temperature peak is shifted toward higher temperatures and the relative shrinkage is enhanced. The third step has a clear trend only the sample aged for 1 h, which the peak position temperature was increased and the peak area was decreased as the calcination temperature was increased. For the fourth step no clear trend could be observed. To summarize, Fig. 7–10 illustrate a multi-stage complex behavior of the third and fourth stage, with respect to aging time and calcinations temperature, which involves a combination of dehydroxylation, decomposition, diffusion and sintering mechanisms.
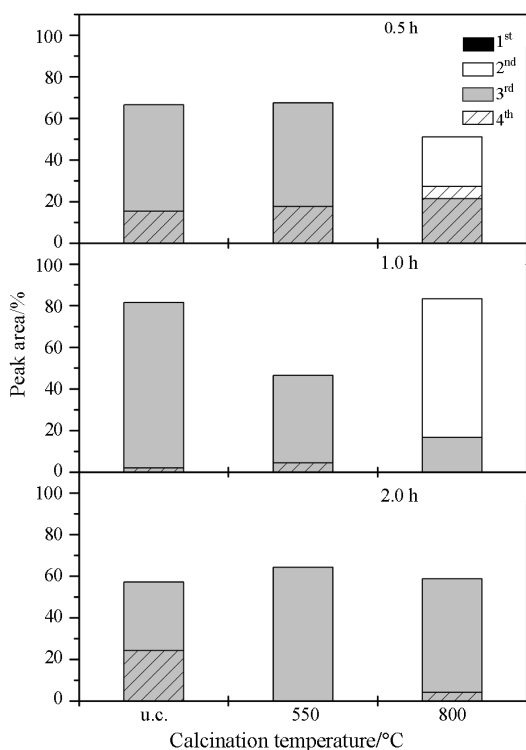
Conclusions

The calcination process strongly affects the properties of nanosized HAp lath-like particles. The particle length is reduced and the particles morphology is changed from lath-like to spherical shape as the calcination temperature is increased. In the same time, the relative density increases. It was found that long aging time favor the formation of thermally stable HAp particles, whereas a shorter one results in the formation of β-calcium phosphate during thermal treatment. Thermal treatment at 1400°C led to the almost complete transformation of HAp to high temperature phase modification –$Ca_3(PO_4)_2$ (α-TCP), while a new phase of $Ca_4(PO_4)O$ appeared. The densification of lath-like HAp has been of own to the complex multistage process including dehydroxylation, decomposition diffusion and sintering mechanisms.

Acknowledgements

Fig. 10 Relative shrinkage during the different stages from Fig. 8 for HAp powders calcined or not at 550 and 800°C. The aging time is indicated

References

1 L. L. Hench, J. Am. Ceram. Soc., 74 (1991) 1487.
2 W. Suchanek and M. Yoshimura, J. Mater. Res., 13 (1998) 94.
3 W. Suchanek and M. Yoshimura, J. Am. Ceram. Soc., 81 (1998) 765.
4 L. Hong, X. Hengchang and K. De Groot, J. Biomed. Mater. Res., 26 (1992) 7.
5 M. Yoshimura and H. Suda, Hydrothermal Processing of Hydroxyapatite: Past, Present and Future. In Hydroxyapatite and Related Materials, Ed. P. W. Brown, and B. Constantz . CRC Press, 1994, pp. 45–52.
6 H. Y. Juang and M. H. Hon, Biomaterials, 17 (1996) 2059.
7 A. K. Burnham, Chem. Eng. J., 108 (2005) 47.
8 Z. He, J. Ma and C. Wang, Biomaterials, 26 (2005) 1613.
9 S. Bailliez and A. Nzihou, Chem. Eng. J., 98 (2004) 141.
10 S. Best and W. Bonfield, J. Mater. Sci.: Mater. Med., 5 (1994) 516.
11 C. Kothapalli, M. Wei, A. Vasiliev and M. T. Shaw, Acta Mater., 52 (2004) 5655.

12 J. Majling, V. Kremničan, R. Durovčíková and Š. Svetík, J. Therm. Anal. Cal., 57 (1999) 587.

13 R. Z. LeGeros and J. P. LeGeros, Dense Hydroxyapatite. In An Introduction to Bioceramics, Ed. L. L. Hench and J. Wilson. World Scientific, Singapore 1993, pp. 139–180.

14 A. Rapacz-Kmita, C. Paluszkiewicz, A. Ślósarczyk and Z. Paszkiewicz, J. Mol. Struct., 744–747 (2005) 653.

15 G. Muralithran and S. Ramesh, Ceram. Int., 26 (2000) 221.

16 N. Y. Mostafa, Mater. Chem. Phys., in press.

17 G. C. Koumoulidis, T. C. Vaimakis, A. T. Sdoukos, N. K. Boukos and C. C. Trapalis, J. Am. Ceram. Soc., 84 (2001) 1203.

18 K. Yamashita and T. Kanazawa, Hydroxyapatite. In Inorganic Phosphate Materials. Materials Science Monography, Vol. 52. Edited by T. Kanazawa. Elsevier Tokyo, Japan, 1989, pp. 15–54.

19 Z. H. Cheng, A. Yasukawa, K. Kandori and T. Ishikawa, J. Chem. Soc. Faraday Trans., 94 (1998) 1501.

20 K. C. Blakeslee and R. A. Condrate, J. Am. Ceram. Soc., 54 (1971) 559.

21 S. Raynaud, E. Champion, D. Bernache-Assollant and P. Thomas, Biomaterials, 23 (2002) 1073.

22 E. Landi, A. Tampieri, G. Celotti and S. Sprio, J. Eur. Ceram. Soc., 20 (2000) 2377.

23 A. J. Ruys, M. Wei, C. C. Sorrell, M. R. Dickson, A. Brandwood and B. K. Milthorpe, Biomaterials, 16 (1995) 409.